



LUND UNIVERSITY

Sensitivity Analysis for Antenna Near-Field Imaging

Nordebo, Sven; Gustafsson, Mats; Persson, Kristin

2005

[Link to publication](#)

Citation for published version (APA):

Nordebo, S., Gustafsson, M., & Persson, K. (2005). *Sensitivity Analysis for Antenna Near-Field Imaging*. (Technical Report LUTEDX/(TEAT-7139)/1-17/(2005); Vol. TEAT-7139). [Publisher information missing].

Total number of authors:

3

General rights

Unless other specific re-use rights are stated the following general rights apply:

Copyright and moral rights for the publications made accessible in the public portal are retained by the authors and/or other copyright owners and it is a condition of accessing publications that users recognise and abide by the legal requirements associated with these rights.

- Users may download and print one copy of any publication from the public portal for the purpose of private study or research.
- You may not further distribute the material or use it for any profit-making activity or commercial gain
- You may freely distribute the URL identifying the publication in the public portal

Read more about Creative commons licenses: <https://creativecommons.org/licenses/>

Take down policy

If you believe that this document breaches copyright please contact us providing details, and we will remove access to the work immediately and investigate your claim.

LUND UNIVERSITY

PO Box 117
221 00 Lund
+46 46-222 00 00

Sensitivity Analysis for Antenna Near-Field Imaging

Sven Nordebo, Mats Gustafsson, and Kristin Persson

Department of Electrosience
Electromagnetic Theory
Lund Institute of Technology
Sweden



Sven Nordebo
Sven.Nordebo@msi.vxu.se

School of Mathematics and Systems Engineering
Växjö University
351 95 Växjö
Sweden

Mats Gustafsson
Mats.Gustafsson@es.lth.se

Department of Electrosience
Electromagnetic Theory
Lund Institute of Technology
P.O. Box 118
SE-221 00 Lund
Sweden

Kristin Persson
Kristin.Persson@es.lth.se

Department of Electrosience
Electromagnetic Theory
Lund Institute of Technology
P.O. Box 118
SE-221 00 Lund
Sweden

Editor: Gerhard Kristensson

© Sven Nordebo, Mats Gustafsson, and Kristin Persson, Lund, October 14, 2005

Abstract

Although imaging and inverse scattering problems have been thoroughly studied during the last century there is only a partial understanding of these complex problems. Most of the efforts have been placed on the development of efficient inversion algorithms and mathematical uniqueness results. In comparison, there are very few results and a limited knowledge about the information content in the inversion data. In this paper, we provide a mathematical framework for sensitivity analysis of imaging problems, based on the multipole expansion of the electromagnetic field and the *Fisher information* to quantify the quality of data. By exploiting this framework, a fundamental uncertainty principle for accuracy and resolution is formulated based on the Cramér-Rao bound. The sensitivity analysis and uncertainty principle for antenna near-field imaging is illustrated using a relevant example with cylindrical measurement data.

1 Introduction

Inverse scattering and imaging are topics with a variety of applications in *e.g.*, medicine, non-destructive testing, surveillance, quantum mechanics, and optics. These problems are in general ill-posed, *i.e.*, they are not well-posed in the sense of existence, uniqueness, and continuous dependence of the solution on the data [2, 5, 9, 12, 15].

The mathematical theory is well developed concerning the uniqueness of inverse scattering problems [9, 12]. The uniqueness theorems typically show that the solution is unique if the data is available from all possible measurements. This is very important but not sufficient from a practical point of view. Further, since the solution of ill-posed problems does not generally depend continuously on the data, the effect of noise on the solution is amplified in a way that calls for proper control. For this purpose, regularization theory [2] is often used to control the imaging error. However, these approaches do not give a qualitative measure on the information content of the inversion data with respect to the accuracy and resolution of images.

Over several decades the Cramér-Rao bound (CRB) has been subjected to many revivals and has become the dominating tool in areas such as statistical signal processing [11], array signal processing [13] and systems and control theory [22]. However, we have observed that estimation theory, the CRB, and maximum likelihood methods [26, 27] are tools that have not been fully exploited in the traditional inverse scattering, imaging or antenna literature.

The CRB provides a lower bound on the estimation error and a fundamental physical limit on system accuracy, but it does not directly indicate the best resolution achievable by an unbiased estimator. Nevertheless, the CRB can be used to define an absolute limit on resolution. In the context of sensor array processing (such as estimation of azimuth, elevation, polarization, etc.) the *statistical resolution limit* is defined as the source separation that equals its own Cramér-Rao bound, providing an algorithm-independent bound on the resolution of any high-resolution method [21].

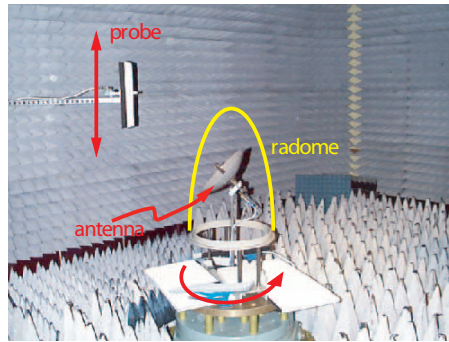


Figure 1: Cylindrical measurement set-up for antenna near-field imaging at SAAB Bofors Dynamics, Sweden.

The purpose of this paper is to provide a mathematical framework for sensitivity analysis of antenna near-field imaging problems, based on the multipole expansion of the electromagnetic field [1, 7, 10], linear estimation theory and the Fisher information [11] to quantify the quality of data, see also [18]. The presented framework has potential for many inverse, or antenna imaging problems such as *e.g.*, in microwave tomography [5], digital holographic microscopy [6], non-destructive testing of wood [20], antenna near-field imaging [19], multimode antenna analysis [23, 29] or as an electromagnetic model for antenna array signal processing using vector sensors [8, 14, 24, 28].

Near-field measurements of antennas are available everywhere today due to their compact set-up and reasonable price. Although they are mainly used to determine the antenna pattern after a near to far-field transformation they have also found application in characterizing the current distribution on antennas and radomes, see *e.g.*, [16, 19, 29]. There are rules of thumb of the set-up of near-field measurements when the far field is wanted. The near-field to equivalent current transformation is more complex and it is necessary to have a qualitative analysis of the associated imaging problem.

As a prototype example of antenna near-field imaging, we study the measurement set-up depicted in Figure 1. The cylindrical data is gathered by rotating the object under test and moving the near-field probe in the vertical direction. By Fourier transforming the data over the azimuthal coordinates the estimation problem decouples and multipoles can be determined from individual systems of linear equations, one for each azimuthal index.

By exploiting the presented framework for sensitivity analysis, we formulate a fundamental uncertainty principle for accuracy and resolution based on the Cramér-Rao bound. In contrast to [21] we retain here the classical definition of resolution and employ the maximum multipole order to quantify the trade-off between accuracy and resolution. Hence, when increasing the desired accuracy (decreasing the desired CRB) in a given measurement set-up, the corresponding resolution of the imaging system is reduced. Numerical examples verify the classical Rayleigh criterion [3], and it is illustrated that superresolution is possible only if the sensor noise (or model

errors) is very small.

The rest of the paper is outlined as follows. In section II follows a detailed description of the prototype example, the inverse multipole problem based on cylindrical data. Section III contains the sensitivity analysis, including both the near and far-field estimation problems. In section IV is formulated the fundamental uncertainty principle for accuracy and resolution. Section V contains numerical examples, and section VI the summary and conclusions. An appendix is also included defining the spherical vector waves and their azimuthal Fourier transforms.

2 The Inverse Multipole Problem based on Cylindrical Data

2.1 Wave Propagation Model and Maximum Mode Order

Throughout the paper, let (r, θ, ϕ) and (ρ, ϕ, z) denote the spherical and cylindrical coordinates, respectively. Further, let $k = \omega/c$ denote the wave number, $\omega = 2\pi f$ the angular frequency, and c and η the speed of light and the wave impedance of free space, respectively.

Assume that all sources are contained inside a sphere of radius $r = a$, and let $e^{i\omega t}$ be the time-convention. The transmitted electric field, $\mathbf{E}(\mathbf{r})$, can then be expanded in *outgoing spherical vector waves* $\mathbf{u}_{\tau ml}(k\mathbf{r})$ for $r > a$ as [1, 7, 10]

$$\mathbf{E}(\mathbf{r}) = \sum_{l=1}^{\infty} \sum_{m=-l}^l \sum_{\tau=1}^2 f_{\tau ml} \mathbf{u}_{\tau ml}(k\mathbf{r}) \quad (2.1)$$

where $f_{\tau ml}$ are the multipole coefficients. Here $\tau = 1$ corresponds to a transversal electric (TE) wave and $\tau = 2$ corresponds to a transversal magnetic (TM) wave. The other indices are $l = 1, 2, \dots, \infty$ and $m = -l \dots, l$ where l denotes the *order* of that mode. It can be shown that in the *far field* when $r \rightarrow \infty$, the electric field is given by $\mathbf{E}(\mathbf{r}) = \frac{e^{-ikr}}{kr} \mathbf{F}(\hat{\mathbf{r}})$ where $\mathbf{F}(\hat{\mathbf{r}})$ is the *far-field amplitude* given by

$$\mathbf{F}(\hat{\mathbf{r}}) = \sum_{l=1}^{\infty} \sum_{m=-l}^l \sum_{\tau=1}^2 i^{l+2-\tau} f_{\tau ml} \mathbf{A}_{\tau ml}(\hat{\mathbf{r}}) \quad (2.2)$$

and where $\mathbf{A}_{\tau ml}(\hat{\mathbf{r}})$ are the *spherical vector harmonics* [1, 7, 10]. For further details about the spherical vector mode representation we refer to the appendix and [1, 7, 10].

In principle, the sum in (2.1) is infinite. However, for all practical purposes the maximum useful order L is finite and can be estimated as follows. The classical theory of radiation Q uses spherical vector modes and equivalent circuits to analyze the properties of a hypothetical antenna inside a sphere, *cf.*, [4]. Hence, by considering an antenna of a given electrical size and normalized bandwidth, we can estimate L by using the Fano broadband matching theory to determine optimum reflection coefficients for each propagating mode, see *e.g.*, [17, 18] with references. However,

the drawback with this approach for practical antennas is that L will most likely be largely overestimated. Instead, we propose here to assess L by employing the uncertainty principle for accuracy and resolution discussed in section IV. With this approach, no a priori knowledge or assumptions about the maximum mode order L is needed. The choice of L is based instead on a Fisher information analysis for the actual measurement set-up and a trade-off between accuracy and resolution.

2.2 Measurement Equation and Inverse Problem

We consider the inverse problem of determining the multipole coefficients $f_{\tau ml}$ based on an observation of the electric near-field $E^p(\mathbf{r}) = \hat{\mathbf{p}}(\mathbf{r}) \cdot \mathbf{E}(\mathbf{r})$ as it is measured on the cylindrical surface $\{\rho = \rho_0, z_1 \leq z \leq z_2\}$ for a given polarization $\hat{\mathbf{p}}(\mathbf{r})$. The inverse multipole problem is fundamental in the sense that it generates estimates for both the near field and the far field, based on the same set of cylindrical measurement data.

Let $\tilde{E}_m^p(\rho, z)$ denote the Discrete Fourier transform (DFT) of the measurement data $E^p(\mathbf{r})$ along the azimuthal coordinate ϕ such that

$$E^p(\mathbf{r}) = \frac{1}{M} \sum_{m=-M/2+1}^{M/2} \tilde{E}_m^p(\rho, z) e^{im\phi} \quad (2.3)$$

where M is the number of azimuthal points and the size of the DFT, $M/2 > L$ and L is assumed to be sufficiently large so that the spatial aliasing in (2.3) can be neglected. The spherical vector waves $\mathbf{u}_{\tau ml}(k\mathbf{r})$ and their corresponding DFT's $\tilde{\mathbf{u}}_{\tau ml}(r, \theta)$ are defined so that $\mathbf{u}_{\tau ml}(k\mathbf{r}) = \tilde{\mathbf{u}}_{\tau ml}(r, \theta) e^{im\phi}$, see the appendix. Hence, by applying the DFT on the input measurement data the fundamental measurement equation decouples and we obtain the following linear system of equations for each m -index of the DFT

$$\frac{1}{M} \tilde{E}_m^p(\rho, z) = \sum_{\tau=1}^2 \sum_{l=\max\{|m|, 1\}}^L f_{\tau ml} \hat{\mathbf{p}}(\mathbf{r}) \cdot \tilde{\mathbf{u}}_{\tau ml}(r, \theta). \quad (2.4)$$

In (2.4), $\hat{\mathbf{p}}(\mathbf{r})$ must be chosen such that $\hat{\mathbf{p}}(\mathbf{r}) \cdot \tilde{\mathbf{u}}_{\tau ml}(r, \theta)$ is independent of ϕ . In a typical (cylindrical) measurement situation, $\hat{\mathbf{p}}(\mathbf{r}) = \hat{\mathbf{z}} = \hat{\mathbf{r}} \cos \theta - \hat{\boldsymbol{\theta}} \sin \theta$ and/or $\hat{\mathbf{p}}(\mathbf{r}) = \hat{\boldsymbol{\phi}}$. Assuming that there are N measurement positions for $\{\rho = \rho_0, z_1 \leq z \leq z_2\}$ and P polarization directions, the fundamental measurement equation (2.4) corresponds to a complex $PN \times 2(L - \max\{|m|, 1\} + 1)$ linear system of equations in the unknowns $f_{\tau ml}$.

In a practical situation, when we wish to estimate the near-field at a sphere of radius $r = a$, it is appropriate to normalize the basis functions $\mathbf{u}_{\tau ml}(k\mathbf{r})$ in (2.1) and (2.4) using the vector norm $\|\mathbf{u}_{\tau ml}(k\mathbf{r})\| = (\int |\mathbf{u}_{\tau ml}(k\mathbf{r})|^2 d\Omega)^{1/2}$ where $d\Omega$ is the differential solid angle and the integration is over the unit sphere. By the

orthonormality of the spherical vector harmonics [1, 7, 10], we have

$$\begin{aligned}\|\mathbf{u}_{1ml}(k\mathbf{r})\|_{r=a}^2 &= \left| h_l^{(2)}(ka) \right|^2 \\ \|\mathbf{u}_{2ml}(k\mathbf{r})\|_{r=a}^2 &= \left| \frac{(kah_l^{(2)}(ka))'}{ka} \right|^2 + l(l+1) \left| \frac{h_l^{(2)}(ka)}{ka} \right|^2\end{aligned}\quad (2.5)$$

where the $(\cdot)'$ indicates differentiation with respect to the argument kr . The purpose of this normalization is to weigh the modes equal, and thus stabilizing the inversion algorithm by improving the conditioning of (2.4). It should be noted however, that the near and far-field estimation problems considered below are *linear* estimation problems and the corresponding Cramér-Rao bounds are invariant to this scaling.

In order to obtain an estimate of the fields, it is assumed that the linear system (2.4) is overdetermined ($PN > 2L$) and solved in the least squares sense. Assuming that the linear system has full rank and that the measurement error is Gaussian, the least squares solution is also the *maximum likelihood* estimate of the multipole coefficients, which is *efficient* in that it attains its Cramér-Rao bound [11]. In practice, however, the linear system is extremely ill-conditioned for large mode orders L and the measurement error may contain non-Gaussian noise as well as non-additive systematic errors. Hence, it is also necessary to regularize the inverse problem by using the Singular Value Decomposition (SVD) and truncate the smallest singular values to avoid excessive noise amplification. Here, we propose also to regularize the inverse problem directly by fixing the maximum useful order L and calculate the corresponding Cramér-Rao bound. The physical meaning of this bound is simply the best possible estimation error for estimating the fields *modulo* the higher order modes (higher order modes excluded).

As a fundamental case we consider a complete vector measurement where $\hat{\mathbf{p}}(\mathbf{r}) = \hat{\mathbf{r}}, \hat{\boldsymbol{\theta}}, \hat{\boldsymbol{\phi}}$, respectively. Denoting by $\tilde{\mathbf{E}}_m(\rho, z) = \hat{\mathbf{r}}\tilde{E}_m^r(\rho, z) + \hat{\boldsymbol{\theta}}\tilde{E}_m^\theta(\rho, z) + \hat{\boldsymbol{\phi}}\tilde{E}_m^\phi(\rho, z)$ we obtain

$$\frac{1}{M}\tilde{\mathbf{E}}_m(\rho, z) = \sum_{\tau=1}^2 \sum_{l=\max\{|m|,1\}}^L f_{\tau ml} \tilde{\mathbf{u}}_{\tau ml}(r, \theta). \quad (2.6)$$

3 Sensitivity Analysis

3.1 Noise Model and Fisher Information

We assume that the measured electric field on the cylinder surface $\mathbf{E}^{(M)}(\mathbf{r})$ is corrupted by additive noise

$$\mathbf{E}^{(M)}(\mathbf{r}) = \mathbf{E}(\mathbf{r}) + \mathbf{N}(\mathbf{r}) \quad (3.1)$$

where $\mathbf{N}(\mathbf{r})$ is a spatially uncorrelated complex Gaussian random process [11] with zero mean and dyadic covariance function

$$\mathcal{E}\{\mathbf{N}(\mathbf{r})\mathbf{N}^*(\mathbf{r}')\} = \sigma_n^2 \delta(\mathbf{r} - \mathbf{r}') \mathbf{I} \quad (3.2)$$

where $\mathcal{E}\{\cdot\}$ denotes the expectation operator, σ_n^2 the noise variance, $\delta(\mathbf{r})$ the impulse function and \mathbf{I} the identity dyad. Note that since the data is assumed here to be discrete, $\delta(\cdot)$ denotes the discrete impulse function with $\delta(0) = 1$.

Denoting by $\widetilde{\mathbf{N}}_m(\rho, z)$ the DFT of the noise term, our signal model is now given by

$$\frac{1}{M}\widetilde{\mathbf{E}}_m^{(M)}(\rho, z) = \sum_{\tau=1}^2 \sum_{l=\max\{|m|,1\}}^L f_{\tau ml} \widetilde{\mathbf{u}}_{\tau ml}(r, \theta) + \frac{1}{M}\widetilde{\mathbf{N}}_m(\rho, z) \quad (3.3)$$

where the covariance of the noise term is

$$\mathcal{E}\left\{\frac{1}{M^2}\widetilde{\mathbf{N}}_m(\rho, z)\widetilde{\mathbf{N}}_{m'}^*(\rho, z')\right\} = \frac{\sigma_n^2}{M}\delta(z - z')\delta(m - m')\mathbf{I}. \quad (3.4)$$

The Fisher information matrix [11] for estimating the multipole coefficients $f_{\tau ml}$ is given by

$$\begin{aligned} [\mathcal{I}]_{\tau ml, \tau' m' l'} &= \frac{M}{\sigma_n^2} \sum_{n=1}^N \frac{\partial \frac{1}{M}\widetilde{\mathbf{E}}_m^*(\rho, z_n)}{\partial f_{\tau ml}^*} \cdot \frac{\partial \frac{1}{M}\widetilde{\mathbf{E}}_{m'}(\rho, z_n)}{\partial f_{\tau' m' l'}} \delta(m - m') = \\ &= \frac{M}{\sigma_n^2} \sum_{n=1}^N \widetilde{\mathbf{u}}_{\tau ml}^*(r_n, \theta_n) \cdot \widetilde{\mathbf{u}}_{\tau' m' l'}(r_n, \theta_n) \delta(m - m') \end{aligned} \quad (3.5)$$

where the indices run over $-L \leq m, m' \leq L$, $\tau, \tau' = 1, 2$, $l = \max\{|m|, 1\}, \dots, L$, and $l' = \max\{|m'|, 1\}, \dots, L$.

The Fisher information matrix is decoupled over the m -index and can hence be organized as a block diagonal matrix with diagonal blocks \mathcal{I}_m with $[\mathcal{I}_m]_{\tau l, \tau' l'} = [\mathcal{I}]_{\tau ml, \tau' m' l'}$ for $-L \leq m \leq L$ where $\tau, \tau' = 1, 2$ and $l, l' = \max\{|m|, 1\}, \dots, L$. Note also that for the block diagonal matrix, $[\mathcal{I}_m^{-1}]_{\tau l, \tau' l'} = [\mathcal{I}^{-1}]_{\tau ml, \tau' m' l'}$.

3.2 Near-Field and Far-Field Estimation

From (2.1), the general Cramér-Rao bound (CRB) [11] for near-field estimation is given by

$$\begin{aligned} \mathcal{E}\{|\mathbf{E}^e(\mathbf{r}) - \mathbf{E}(\mathbf{r})|^2\} &\geq \sum_{l=1}^L \sum_{m=-l}^l \sum_{\tau=1}^2 \sum_{l'=1}^L \sum_{m'=-l'}^{l'} \sum_{\tau'=1}^2 \cdots \\ &\cdots [\mathcal{I}^{-1}]_{\tau ml, \tau' m' l'} \mathbf{u}_{\tau ml}^*(k\mathbf{r}) \cdot \mathbf{u}_{\tau' m' l'}(k\mathbf{r}) \end{aligned} \quad (3.6)$$

where $\mathbf{E}^e(\mathbf{r})$ denotes the estimated field and \mathcal{I}^{-1} is the inverse of the Fisher information matrix. Generally, the CRB in (3.6) is a scalar field depending on all the three spatial coordinates (r, θ, ϕ) .

Since the Fisher information (3.5) is decoupled over the m -index, the corresponding CRB (3.6) becomes

$$\begin{aligned} \mathcal{E}\{|\mathbf{E}^e(\mathbf{r}) - \mathbf{E}(\mathbf{r})|^2\} &\geq \sum_{m=-L}^L \sum_{\tau=1}^2 \sum_{l=\max\{|m|,1\}}^L \sum_{\tau'=1}^2 \sum_{l'=\max\{|m|,1\}}^L \cdots \\ &\cdots [\mathcal{I}_m^{-1}]_{\tau l, \tau' l'} \widetilde{\mathbf{u}}_{\tau ml}^*(r, \theta) \cdot \widetilde{\mathbf{u}}_{\tau' m' l'}(r, \theta) \end{aligned} \quad (3.7)$$

where we have employed $\mathbf{u}_{\tau ml}(k\mathbf{r}) = \tilde{\mathbf{u}}_{\tau ml}(r, \theta)e^{im\phi}$. Note that the CRB in (3.7) is independent of the azimuthal coordinate ϕ , and depends only on (r, θ) .

The sensitivity analysis for the far field $\mathbf{F}(\hat{\mathbf{r}})$ in (2.2) is obtained from the previous results simply by replacing $\mathbf{u}_{\tau ml}(k\mathbf{r})$ in (3.6) by $i^{-l-2+\tau}\mathbf{A}_{\tau ml}(\hat{\mathbf{r}})$. Hence, the general CRB for estimating $\mathbf{F}(\hat{\mathbf{r}})$ is given by

$$\begin{aligned} \mathcal{E}\{|\mathbf{F}^e(\hat{\mathbf{r}}) - \mathbf{F}(\hat{\mathbf{r}})|^2\} &\geq \sum_{l=1}^L \sum_{m=-l}^l \sum_{\tau=1}^2 \sum_{l'=1}^L \sum_{m'=-l'}^{l'} \sum_{\tau'=1}^2 \cdots \\ &\cdots [\mathcal{I}^{-1}]_{\tau l, \tau' m' l'} i^{l-l'} i^{\tau'-\tau} \mathbf{A}_{\tau ml}^*(\hat{\mathbf{r}}) \cdot \mathbf{A}_{\tau' m' l'}(\hat{\mathbf{r}}) \end{aligned} \quad (3.8)$$

which depends generally on both directional coordinates (θ, ϕ) .

Since the Fisher information (3.5) is decoupled over the m -index, the corresponding CRB (3.8) becomes

$$\begin{aligned} \mathcal{E}\{|\mathbf{F}^e(\hat{\mathbf{r}}) - \mathbf{F}(\hat{\mathbf{r}})|^2\} &\geq \sum_{m=-L}^L \sum_{\tau=1}^2 \sum_{l=\max\{|m|, 1\}}^L \sum_{\tau'=1}^2 \sum_{l'=\max\{|m|, 1\}}^L \cdots \\ &\cdots [\mathcal{I}_m^{-1}]_{\tau l, \tau' l'} i^{l-l'} i^{\tau'-\tau} \tilde{\mathbf{A}}_{\tau ml}^*(\theta) \cdot \tilde{\mathbf{A}}_{\tau' m l'}(\theta) \end{aligned} \quad (3.9)$$

where we have employed $\mathbf{A}_{\tau ml}(\hat{\mathbf{r}}) = \tilde{\mathbf{A}}_{\tau ml}(\theta)e^{im\phi}$. Note that the CRB in (3.9) is independent of the azimuthal coordinate ϕ , and depends only on the elevation θ .

4 Uncertainty Principle for Accuracy and Resolution

The resolution capability associated with the antenna near-field imaging problem is determined by the maximum useful order L . At the same time, the maximum mode order L gives a limit for the best possible estimation accuracy via the Cramér-Rao bound (3.6). Hence, there is a fundamental connection between the accuracy (optimum estimation performance) and the resolution capability of an imaging system, a connection which can be phrased as an *uncertainty principle for accuracy and resolution*.

Consider first the resolution capability associated with the maximum useful order L . Assume that we wish to image an idealized far field (2.2) with uncorrelated, zero mean and unit variance multipole coefficients $\mathcal{E}\{f_{\tau ml}f_{\tau ml}^*\} = \delta_{\tau\tau'}\delta_{mm'}\delta_{ll'}$. The covariance dyadic of this field is readily seen to be given by

$$\mathcal{E}\{\mathbf{F}(\hat{\mathbf{r}})\mathbf{F}^*(\hat{\mathbf{r}}')\} = \sum_{l=1}^{\infty} \sum_{m=-l}^l \sum_{\tau=1}^2 \mathbf{A}_{\tau ml}(\hat{\mathbf{r}})\mathbf{A}_{\tau ml}^*(\hat{\mathbf{r}}') = \delta(\hat{\mathbf{r}} - \hat{\mathbf{r}}')\mathbf{I} \quad (4.1)$$

where the second equality follows from a multipole expansion of $\delta(\hat{\mathbf{r}} - \hat{\mathbf{r}}')\mathbf{I}$ where $\delta(\cdot)$ is the impulse function on the unit sphere and \mathbf{I} is the unit dyad. Hence, the covariance dyadic can be interpreted as a spatial impulse at position $\hat{\mathbf{r}}'$.

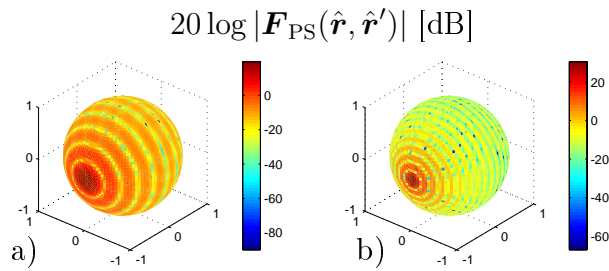


Figure 2: The two-dimensional point spread function $\mathbf{F}_{\text{PS}}(\hat{\mathbf{r}}, \hat{\mathbf{r}}')$ for $\theta' = \pi/2$ and $\phi' = \pi$. a) Mode order $L = 10$. b) Mode order $L = 20$.

We define the two-dimensional *point spread function* [25] $\mathbf{F}_{\text{PS}}(\hat{\mathbf{r}}, \hat{\mathbf{r}}')$ as the right θ (or ϕ) component of (4.1) truncated to order L as

$$\mathbf{F}_{\text{PS}}(\hat{\mathbf{r}}, \hat{\mathbf{r}}') = \sum_{l=1}^L \sum_{m=-l}^l \sum_{\tau=1}^2 \mathbf{A}_{\tau ml}(\hat{\mathbf{r}}) \tilde{A}_{\tau ml}^{\theta*}(\theta') e^{-im\phi'} \quad (4.2)$$

corresponding to an L order multipole expansion of the impulse vector field $\hat{\boldsymbol{\theta}}' \delta(\hat{\mathbf{r}} - \hat{\mathbf{r}}')$ (or $\hat{\boldsymbol{\phi}}' \delta(\hat{\mathbf{r}} - \hat{\mathbf{r}}')$) positioned at $\hat{\mathbf{r}}'$. The magnitude of $\mathbf{F}_{\text{PS}}(\hat{\mathbf{r}}, \hat{\mathbf{r}}')$ is shown in Figure 2 for $\theta' = \pi/2$, $\phi' = \pi$ and $L = 10, 20$ respectively, illustrating the correlation properties of the truncated random vector field described above.

It is observed that the shape of the magnitude of the two-dimensional point spread function $|\mathbf{F}_{\text{PS}}(\hat{\mathbf{r}}, \hat{\mathbf{r}}')|$ illustrated in Figure 2 is invariant to the choice of position (rotation) (θ', ϕ') as well as of the polarization, *i.e.*, choice of right θ or ϕ component of (4.1), *cf.*, [7] for a reference to the rotational properties of the spherical vector waves. Hence, the resolution capability in both θ and ϕ coordinates are given by the one-dimensional point spread function

$$F_{\text{PS}}^{\theta}(\phi) = \hat{\boldsymbol{\theta}} \cdot \mathbf{F}_{\text{PS}}(\hat{\mathbf{r}}, \hat{\mathbf{r}}') \Big|_{\theta=\frac{\pi}{2}, \theta'=\frac{\pi}{2}, \phi'=0} = \sum_{m=-L}^L c_m e^{im\phi} \quad (4.3)$$

where

$$c_m = \sum_{\tau=1}^2 \sum_{l=\max\{|m|, 1\}}^L \left| \tilde{A}_{\tau ml}^{\theta}\left(\frac{\pi}{2}\right) \right|^2 \quad (4.4)$$

are the Fourier series coefficients of $F_{\text{PS}}^{\theta}(\phi)$. The one-dimensional point spread function $F_{\text{PS}}^{\theta}(\phi)$ is shown in Figure 3 where $L = 15, 30, 60$.

The classical measure of resolution is given by the width of the mainlobe of the point spread function, defined here by the first zero of $F_{\text{PS}}^{\theta}(\phi)$, *cf.*, Figure 3. The resolution is hence roughly the same as of the rectangular window, *i.e.*,

$$\Delta\phi \sim k \frac{2\pi}{2L+1} \quad (4.5)$$

where $k = 1$ for the rectangular window and $k \approx 1.2$ for the one-dimensional point spread function $F_{\text{PS}}^{\theta}(\phi)$.

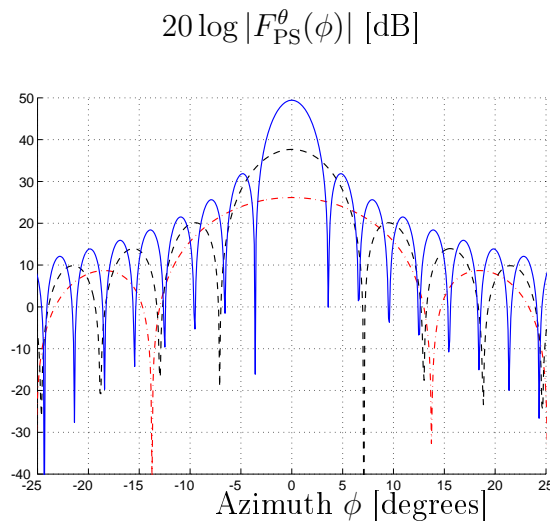


Figure 3: The one-dimensional point spread function $F_{\text{PS}}^{\theta}(\phi)$ for $\theta = \pi/2$, $\theta' = \pi/2$ and $\phi' = 0$. Maximum mode orders are $L = 15, 30, 60$.

For a given measurement set-up, (3.6) and (4.5) define a one-to-one relation between the CRB and the resolution $\Delta\phi$ via the parameter L . Since the CRB is a lower bound, this relation represents a feasible region and an *uncertainty principle for accuracy and resolution*. An illustration of this principle is given in the next section.

5 Numerical Examples

In order to illustrate the sensitivity analysis we employ as a numerical example a measurement situation and data taken from an industrial measurement campaign¹ performed for a 8 GHz radar antenna ($\lambda = 3.75$ cm).

The input data for the antenna near-field imaging problem was acquired in an anechoic chamber using a cylindrical measurement set-up as depicted in Figure 1. The data was collected in $M = 120$ azimuthal points and $N = 129$ vertical positions for $-0.8 = z_1 \leq z \leq z_2 = 0.8$ and $\rho_0 = 0.459$ (all units in [m]).

The inverse problem in Equation (2.4) was solved using the normalized basis functions $\frac{\tilde{\mathbf{u}}_{rmi}(r, \theta)}{\|\mathbf{u}_{rmi}(k\mathbf{r})\|_{r=a}}$, maximum mode order $L = 59$ and regularization of the least squares problem by truncating the singular values less than unity. The spherical coordinate system was centered at $z = -0.35$, where the antenna was approximately situated. The resulting near-field estimation is shown in Figure 4 for $0.30 \leq r \leq 1.38$, $0 \leq \theta \leq \pi$ and $\phi = (0, \pi)$ (xz -plane).

The sensitivity analysis addresses the question how, when and where the near-field estimation is reliable. In the analysis below, we define the Signal to Noise Ratio

¹The measurement campaign was performed by SAAB Bofors Dynamics and Chelton Applied Composites, Sweden.

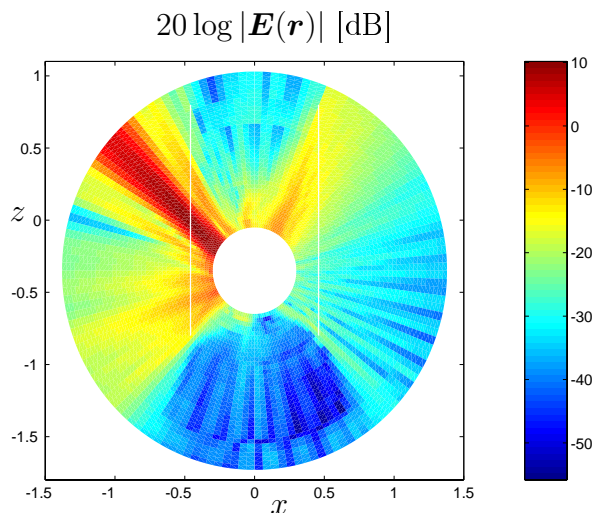


Figure 4: Spherical near-field estimation from cylindrical data. Nearfield of an 8 GHz antenna plotted in the xz -plane. The measurement cylinder is indicated with white lines.

(SNR) as

$$\text{SNR} = \frac{\max_{\text{meas}} |\mathbf{E}(\mathbf{r})|^2}{\sigma_n^2} \quad (5.1)$$

where $\max_{\text{meas}} |\mathbf{E}(\mathbf{r})|^2$ is the maximum electric field strength over all measurement points and σ_n^2 the variance of the measurement noise. In all the examples below, the Cramér-Rao bounds are calculated for $\text{SNR} = 100$ dB. In Figure 5 is shown the Cramér-Rao bound (3.7) using maximum mode order² $L = 59$. The Cramér-Rao bound is here a two dimensional scalar field, independent of the azimuthal coordinate ϕ due to the rotational symmetry of the problem. Note that the cylindrical shape of the measurement surface is clearly visible in Figure 5. Since the maximum measured field strength is about 5 dB, it is concluded from Figure 5 that near-field estimation using $L = 59$ is feasible with high or acceptable accuracy in the blue and green areas, whereas estimation is not feasible at all in the red areas.

Next, we consider the far-field estimation problem based on cylindrical data. In Figure 6 is shown the far-field amplitude (2.2) corresponding to the multipoles which are calculated for the near-field inverse problem at radius $r = 1.38$. The maximum far-field amplitude is about 50 dB. In Figure 7 is shown the one dimensional Cramér-Rao bound (3.9) as a function of elevation θ for various maximum mode orders L . The analysis shows that the far-field estimation is feasible with high accuracy using mode orders up to $L = 60$, provided that the elevation angles are within the range 40 to 90 degrees. The poor estimation performance obtained outside this region is due to the finite extent of the cylinder measurement.

Finally, we conclude the examples by illustrating the uncertainty principle for accuracy and resolution described in section 4. Let $\text{CRB}(r, \theta)$ denote the Cramér-

²The parameter values $L = 59$ and $\text{SNR} = 100$ dB are not optimized for this measurement and are chosen merely for illustration purposes.

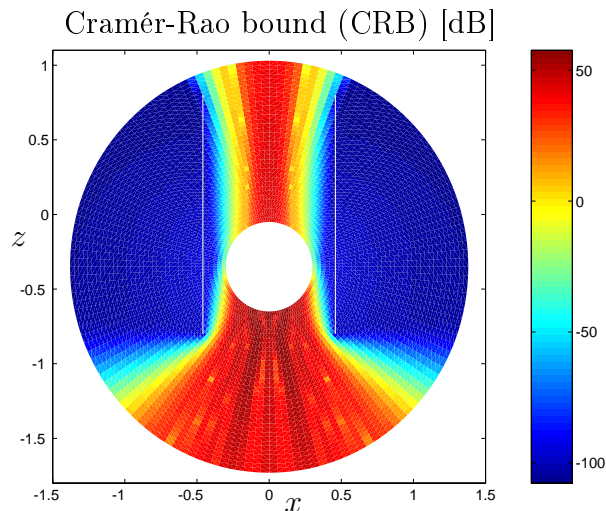


Figure 5: Cramér-Rao bound for the example near-field problem. The plot is shown in the xz -plane, and is rotationally symmetrical about the z -axis. Maximum mode order is $L = 59$. The measurement cylinder is indicated with white lines. Estimation is feasible in the blue and green areas.

Rao bound given by (3.7) and define the relative accuracy by

$$\overline{\text{CRB}}(r, \theta) = \frac{\text{CRB}(r, \theta)}{\sigma_n^2} \quad (5.2)$$

where σ_n^2 is the variance of the measurement noise. For each value of the maximum order L , the expressions (3.7) and (4.5) define a one-to-one relation between the relative accuracy $\overline{\text{CRB}}(r, \theta)$ and the resolution $\Delta\phi$. The resulting mapping is illustrated in Figure 8 for $r = 0.3, 1.5, \infty$ and $\theta = 1, 10, 20, 30, 40, 80$ degrees. Note that the plot has been generated by using parameter values $L = 1, \dots, 50$. Observe also that for the far-field case $r = \infty$, we have used (3.9) to define the CRB with different scaling for the far-field amplitude. The plot illustrates the trade-off between accuracy and resolution. Note that the resolution (or accuracy) is very poor for $\theta = 1$ degree which is far outside the span of the cylinder, and improves systematically for the elevation angles between 1 and 80 degrees, *cf.*, Figure 7.

Figure 9 shows the normalized resolution $r\Delta\phi/\lambda$ as a function of relative accuracy $\overline{\text{CRB}}$ for $r = 0.3, 1.5$ m and $\theta = 10, 20, 80$ degrees. The plot illustrates that the normalized resolution (in units of wavelengths) is better for smaller radius. Note that even though $r\Delta\phi/\lambda$ seem to approach the classical $\lambda/2$ Rayleigh limit as $\overline{\text{CRB}}$ increases, superresolution $r\Delta\phi/\lambda < \frac{1}{2}$ is in principle possible. However, the cost of achieving superresolution is very poor relative accuracy $\overline{\text{CRB}}$ which is acceptable only if the sensor noise σ_n^2 is very low.

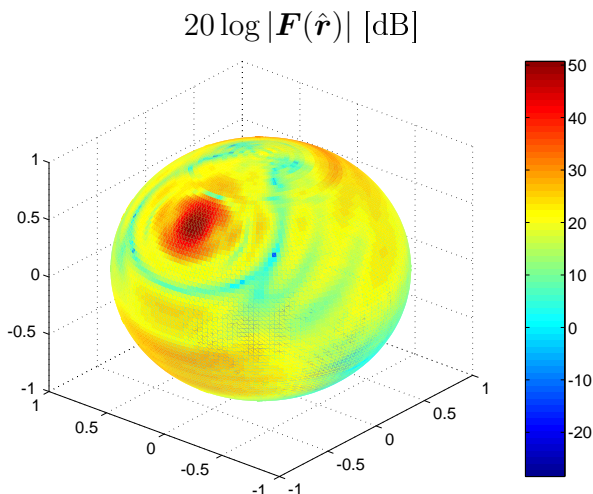


Figure 6: Spherical far-field estimation from cylindrical data. Far field of an 8 GHz antenna plotted on the unit sphere.

6 Summary and Conclusions

A mathematical framework for sensitivity analysis of inverse scattering problems is given based on the *Fisher information* and the multipole expansion of the electromagnetic field. The sensitivity analysis for antenna near-field imaging is performed using a relevant example with cylindrical near-field measurement data. The Cramér-Rao bound is used to quantify the ill-conditioning of the inverse problem, and the bound is shown to be a very useful tool for visualizing and understanding the physics of the inverse problem. In particular, we show that there is a fundamental connection between the accuracy (optimum estimation performance) and the resolution capability of an imaging system, a connection which can be phrased as an uncertainty principle for accuracy and resolution.

Acknowledgement

The authors like to express their gratitude to SAAB Bofors Dynamics, Sweden, and especially to Michael Andersson and Sören Poulsen at Chelton Applied Composites, Sweden, for supplying the near-field data and pictures of the experimental set-up. The second and third authors also gratefully acknowledge the financial support by Försvarets Materielverk (FMV), Sweden.

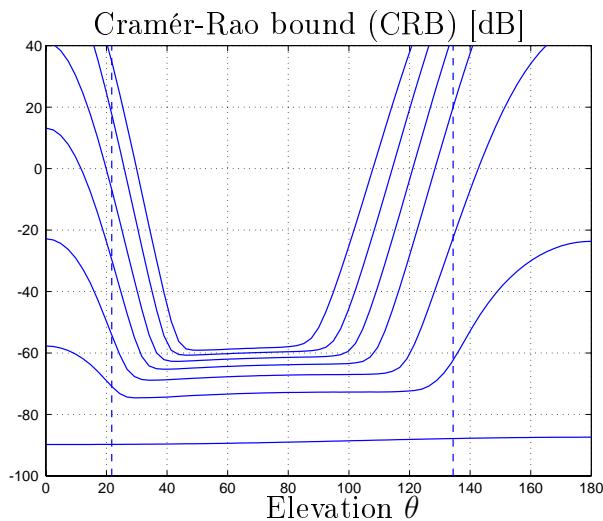


Figure 7: Cramér-Rao bound for the example far-field problem, plotted as a function of elevation θ . Maximum mode orders are $L = 1, 10, 20, 30, 40, 50$ and 60 . The span of the cylinder is indicated by the horizontal dashed lines.

Appendix A Spherical Vector Waves and their Azimuthal Fourier Transforms

The outgoing spherical vector waves are given by

$$\begin{aligned} \mathbf{u}_{1ml}(k\mathbf{r}) &= h_l^{(2)}(kr) \mathbf{A}_{1ml}(\hat{\mathbf{r}}) \\ \mathbf{u}_{2ml}(k\mathbf{r}) &= \frac{1}{k} \nabla \times \mathbf{u}_{1ml}(k\mathbf{r}) = \\ &= \frac{(kr h_l^{(2)}(kr))'}{kr} \mathbf{A}_{2ml}(\hat{\mathbf{r}}) + \sqrt{l(l+1)} \frac{h_l^{(2)}(kr)}{kr} \mathbf{A}_{3ml}(\hat{\mathbf{r}}) \end{aligned} \quad (\text{A.1})$$

where $\mathbf{A}_{\tau ml}(\hat{\mathbf{r}})$ are the *spherical vector harmonics* and $h_l^{(2)}(x)$ the *spherical Hankel functions of the second kind*, see [1, 7, 10]. The spherical vector harmonics $\mathbf{A}_{\tau ml}(\hat{\mathbf{r}})$ are given by

$$\begin{aligned} \mathbf{A}_{1ml}(\hat{\mathbf{r}}) &= \frac{1}{\sqrt{l(l+1)}} \nabla \times (\mathbf{r} Y_{ml}(\hat{\mathbf{r}})) \\ \mathbf{A}_{2ml}(\hat{\mathbf{r}}) &= \hat{\mathbf{r}} \times \mathbf{A}_{1ml}(\hat{\mathbf{r}}) \\ \mathbf{A}_{3ml}(\hat{\mathbf{r}}) &= \hat{\mathbf{r}} Y_{ml}(\hat{\mathbf{r}}) \end{aligned} \quad (\text{A.2})$$

where $Y_{ml}(\hat{\mathbf{r}})$ are the scalar *spherical harmonics* given by

$$Y_{ml}(\theta, \phi) = (-1)^m \sqrt{\frac{2l+1}{4\pi}} \sqrt{\frac{(l-m)!}{(l+m)!}} P_l^m(\cos \theta) e^{im\phi} \quad (\text{A.3})$$

and where $P_l^m(x)$ are the *associated Legendre functions* [1]. For negative m -indices, the scalar waves satisfies the symmetry $Y_{-m,l}(\hat{\mathbf{r}}) = (-1)^m Y_{ml}^*(\hat{\mathbf{r}})$, and hence

$$\mathbf{A}_{\tau,-m,l}(\hat{\mathbf{r}}) = (-1)^m \mathbf{A}_{\tau ml}^*(\hat{\mathbf{r}}). \quad (\text{A.4})$$

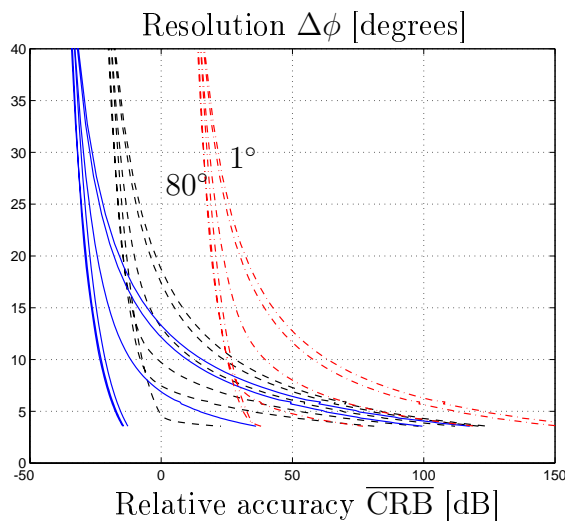


Figure 8: Resolution $\Delta\phi$ as a function of relative accuracy $\overline{\text{CRB}}$. Solid blue line: $r = 1.5$ m. Dashed black line: $r = 0.3$ m. Dash-dotted red line: far field $r = \infty$. Elevation angles are: $\theta = 1, 10, 20, 30, 40, 80$ degrees.

For convenience, we introduce also the *normalized* associated Legendre functions

$$\bar{P}_l^m(x) = \sqrt{\frac{2l+1}{2}} \sqrt{\frac{(l-m)!}{(l+m)!}} P_l^m(x) \quad (\text{A.5})$$

so that $Y_{ml}(\hat{\mathbf{r}}) = (-1)^m \bar{P}_l^m(\cos\theta) \frac{1}{\sqrt{2\pi}} e^{im\phi}$. The following relations for $\bar{P}_l^m(x)$ are useful for numerical calculations

$$\begin{aligned} \bar{P}_l^{-m}(x) &= (-1)^m \bar{P}_l^m(x) \\ \frac{\partial}{\partial\theta} \bar{P}_l^m(\cos\theta) &= \frac{1}{2} \sqrt{(l+m)(l-m+1)} \bar{P}_l^{m-1}(\cos\theta) \\ &\quad - \frac{1}{2} \sqrt{(l+m+1)(l-m)} \bar{P}_l^{m+1}(\cos\theta). \end{aligned} \quad (\text{A.6})$$

Note also that $\bar{P}_l^m(x) = 0$ for $m > l$.

Now, from (A.2) the spherical vector harmonics may be derived as

$$\begin{aligned} \mathbf{A}_{1ml}(\hat{\mathbf{r}}) &= \tilde{\mathbf{A}}_{1ml}(\theta) e^{im\phi} = \\ &= \frac{(-1)^m}{\sqrt{l(l+1)}} \left(\hat{\boldsymbol{\theta}} \frac{im}{\sin\theta} \bar{P}_l^m(\cos\theta) - \hat{\boldsymbol{\phi}} \frac{\partial}{\partial\theta} \bar{P}_l^m(\cos\theta) \right) \frac{1}{\sqrt{2\pi}} e^{im\phi} \\ \mathbf{A}_{2ml}(\hat{\mathbf{r}}) &= \tilde{\mathbf{A}}_{2ml}(\theta) e^{im\phi} = \\ &= \frac{(-1)^m}{\sqrt{l(l+1)}} \left(\hat{\boldsymbol{\theta}} \frac{\partial}{\partial\theta} \bar{P}_l^m(\cos\theta) + \hat{\boldsymbol{\phi}} \frac{im}{\sin\theta} \bar{P}_l^m(\cos\theta) \right) \frac{1}{\sqrt{2\pi}} e^{im\phi} \\ \mathbf{A}_{3ml}(\hat{\mathbf{r}}) &= \tilde{\mathbf{A}}_{3ml}(\theta) e^{im\phi} = \hat{\mathbf{r}} (-1)^m \bar{P}_l^m(\cos\theta) \frac{1}{\sqrt{2\pi}} e^{im\phi} \end{aligned} \quad (\text{A.7})$$

where the *Fourier transformed* spherical vector harmonics $\tilde{\mathbf{A}}_{\tau ml}(\theta)$ are defined so that

$$\mathbf{A}_{\tau ml}(\hat{\mathbf{r}}) = \tilde{\mathbf{A}}_{\tau ml}(\theta) e^{im\phi}. \quad (\text{A.8})$$

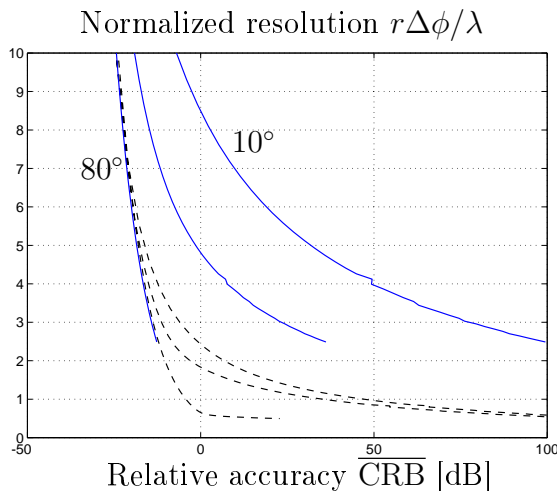


Figure 9: Normalized resolution $r\Delta\phi/\lambda$ as a function of relative accuracy $\overline{\text{CRB}}$. Solid blue line: $r = 1.5$ m. Dashed black line: $r = 0.3$ m. Elevation angles are: $\theta = 10, 20, 80$ degrees.

The Fourier transformed outgoing spherical vector waves $\tilde{\mathbf{u}}_{\tau ml}(r, \theta)$ are derived similarly from (A.1) as

$$\begin{aligned} \tilde{\mathbf{u}}_{1ml}(r, \theta) &= h_l^{(2)}(kr) \tilde{\mathbf{A}}_{1ml}(\theta) \\ \tilde{\mathbf{u}}_{2ml}(r, \theta) &= \\ & \frac{(kr h_l^{(2)}(kr))'}{kr} \tilde{\mathbf{A}}_{2ml}(\theta) + \sqrt{l(l+1)} \frac{h_l^{(2)}(kr)}{kr} \tilde{\mathbf{A}}_{3ml}(\theta) \end{aligned} \quad (\text{A.9})$$

so that

$$\mathbf{u}_{\tau ml}(k\mathbf{r}) = \tilde{\mathbf{u}}_{\tau ml}(r, \theta) e^{im\phi}. \quad (\text{A.10})$$

Note that $\tilde{\mathbf{A}}_{\tau ml}(\theta)$ and $\tilde{\mathbf{u}}_{\tau ml}(r, \theta)$ are defined as Fourier transforms only with respect to their respective spherical r, θ, ϕ components. As vector fields they still depend on the ϕ coordinate via the basis vectors $\hat{\mathbf{r}}, \hat{\boldsymbol{\theta}}, \hat{\boldsymbol{\phi}}$.

References

- [1] G. B. Arfken and H. J. Weber. *Mathematical Methods for Physicists*. Academic Press, New York, fifth edition, 2001.
- [2] M. Bertero. Linear inverse and ill-posed problems. *Advances in electronics and electron physics*, **75**, 1–120, 1989.
- [3] M. Born and E. Wolf. *Principles of Optics*. Cambridge University Press, Cambridge, U.K., seventh edition, 1999.
- [4] R. E. Collin and S. Rothschild. Evaluation of antenna Q. *IEEE Trans. Antennas Propagat.*, **12**, 23–27, January 1964.

- [5] M. Gustafsson. *Wave Splitting in Direct and Inverse Scattering Problems*. PhD thesis, Lund Institute of Technology, Department of Electromagnetic Theory, P.O. Box 118, S-221 00 Lund, Sweden, 2000.
<http://www.es.lth.se/home/mats>.
- [6] M. Gustafsson, M. Sebesta, B. Bengtsson, S.-G. Pettersson, P. Egelberg, and T. Lenart. High resolution digital transmission microscopy—a fourier holography approach. *Optics and Lasers in Engineering*, **41**(3), 553–563, 2004.
- [7] J. E. Hansen, editor. *Spherical Near-Field Antenna Measurements*. Number 26 in IEE electromagnetic waves series. Peter Peregrinus Ltd., Stevenage, UK, 1988. ISBN: 0-86341-110-X.
- [8] K.-C. Ho, K.-C. Tan, and A. Nehorai. Estimating directions of arrival of completely and incompletely polarized signals with electromagnetic vector sensors. *IEEE Trans. Signal Process.*, **47**(10), 2845–2852, October 1999.
- [9] V. Isakov. *Inverse Problems for Partial Differential Equations*. Springer-Verlag, Berlin, 1998.
- [10] J. D. Jackson. *Classical Electrodynamics*. John Wiley & Sons, New York, second edition, 1975.
- [11] S. M. Kay. *Fundamentals of Statistical Signal Processing, Estimation Theory*. Prentice-Hall, Inc., NJ, 1993.
- [12] A. Kirsch. *An Introduction to the Mathematical Theory of Inverse Problems*. Springer-Verlag, New York, 1996.
- [13] H. Krim and M. Viberg. Two decades of array signal processing research: the parametric approach. *IEEE Signal Processing Magazine*, **13**(4), 67–94, July 1996.
- [14] J. Li and P. Stoica. Efficient parameter estimation of partially polarized electromagnetic waves. *IEEE Trans. Signal Process.*, **42**(11), 3114–3125, November 1994.
- [15] E. A. Marengo and R. W. Ziolkowski. Nonradiating and minimum energy sources and their fields: Generalized source inversion theory and applications. *IEEE Trans. Antennas Propagat.*, **48**(10), 1553–1562, October 2000.
- [16] R. U. Nair and R. M. Jha. Tuning of EM performance for streamlined aircraft radomes. In *2004 IEEE Antennas and Propagation Society Symposium*, volume 1, pages 874–877. IEEE Antennas and Propagation Society, 2004.
- [17] S. Nordebo and M. Gustafsson. Multichannel broadband Fano theory for arbitrary lossless antennas with applications in DOA estimation. In *2005 IEEE International Conference on Acoustics, Speech, and Signal Processing*, volume IV, pages 969–972, 2005.

- [18] S. Nordebo and M. Gustafsson. Statistical signal analysis for the inverse source problem of electromagnetics. Technical Report LUTEDX/(TEAT-7136)/1-12/(2005), Lund Institute of Technology, Department of Electrosience, P.O. Box 118, S-211 00 Lund, Sweden, 2005. <http://www.es.lth.se/teore1>, Accepted by IEEE Trans. Signal Process.
- [19] K. Persson and M. Gustafsson. Reconstruction of equivalent currents using a near-field data transformation – with radome applications. *Progress in Electromagnetics Research*, **54**, 179–198, 2005.
- [20] T. Sjöden, S. Nordebo, and B. Nilsson. Microwave modelling and measurements for early detection of spiral grain in wood. In *14th International Symposium on Nondestructive Testing of Wood*. Eberswalde, Germany, 2005.
- [21] S. T. Smith. Statistical resolution limits and the complexified Cramér–Rao bound. *IEEE Trans. Signal Process.*, **53**(5), 1597–1609, May 2005.
- [22] T. Söderström and P. Stoica. *System Identification*. Prentice Hall, 2001.
- [23] T. Svantesson, M. A. Jensen, and J. W. Wallace. Analysis of electromagnetic field polarizations in multiantenna systems. *IEEE Transactions on Wireless Communications*, **3**(2), 641–646, March 2004.
- [24] A. Swindlehurst and M. Viberg. Subspace fitting with diversely polarized antenna arrays. *IEEE Trans. Antennas Propagat.*, **41**(12), 1687–1694, December 1993.
- [25] A. R. Thompson, J. M. Moran, and G. W. Swenson. *Interferometry and Synthesis in Radio Astronomy*. John Wiley & Sons, Inc., second edition, 2001.
- [26] M. Viberg, P. Stoica, and B. Ottersten. Maximum likelihood array processing in spatially correlated noise fields using parameterized signals. *IEEE Trans. Signal Process.*, **45**(4), 996–1004, April 1997.
- [27] A. J. Weiss and B. Friedlander. Maximum likelihood signal estimation for polarization sensitive arrays. *IEEE Trans. Antennas Propagat.*, **41**(7), 918–925, July 1993.
- [28] K. T. Wong and M. D. Zoltowski. Closed-form direction finding and polarization estimation with arbitrarily spaced electromagnetic vector-sensors at unknown locations. *IEEE Trans. Antennas Propagat.*, **48**(5), 671–681, May 2000.
- [29] A. D. Yaghjian. An overview of near-field antenna measurements. *IEEE Trans. Antennas Propagat.*, **34**(1), 30–45, January 1986.